IEEE Photonics Journal
An IEEE Photonics Society Publication

Open Access

Tandem Electrooptic Modulation and Interferometric Detection: Theory and Application

Volume 5, Number 4, August 2013

Sharon R. Harmon, Member, IEEE
Vincent J. Urick, Senior Member, IEEE
John F. Diehl
Keith J. Williams, Member, IEEE

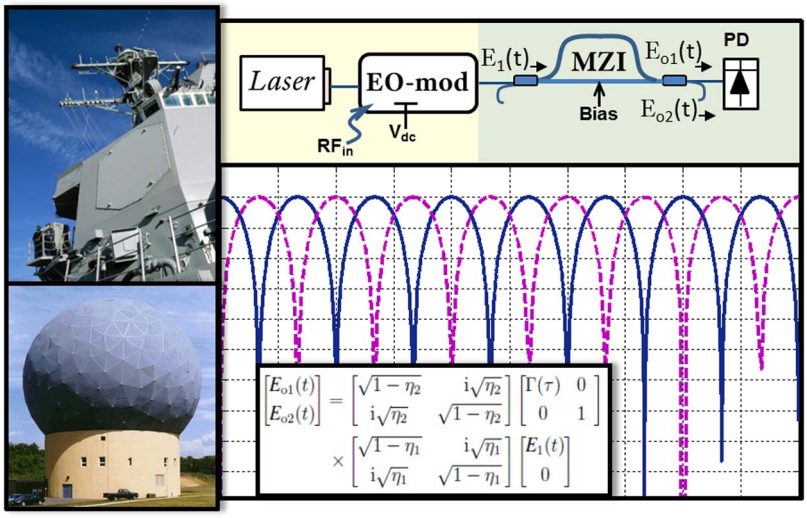

DOI: 10.1109/JPHOT.2013.2271899
1943-0655/$31.00 ©2013 IEEE

IEEE photonics SOCIETY

IEEE

Tandem Electrooptic Modulation and Interferometric Detection: Theory and Application

Sharon R. Harmon,[1] *Member, IEEE*, Vincent J. Urick,[2] *Senior Member, IEEE*, John F. Diehl,[2] and Keith J. Williams,[2] *Member, IEEE*

[1]Sotera Defense Solutions, Inc., Herndon, VA 20171-5393 USA
[2]U.S. Naval Research Laboratory, Washington, DC 20375 USA

DOI: 10.1109/JPHOT.2013.2271899
1943-0655/$31.00 ©2013 IEEE

Manuscript received May 20, 2013; revised June 18, 2013; accepted June 18, 2013. Date of publication July 3, 2013; date of current version July 19, 2013. Corresponding author: S. R. Harmon (e-mail: sharon.harmon.ctr@nrl.navy.mil).

Abstract: This paper expands upon the RF photonic theory of electrooptic phase and intensity modulation detection as seen when coupled in tandem with an asymmetric Mach–Zehnder interferometer through the derivation of power transfer functions for such optical-microwave configurations. An inspection of the theory is presented and validated through experimental results. Several applications of a modulation/interferometric architecture are also reviewed, delineating the importance of a valid model for predicting the behavior of similar analog optical systems.

Index Terms: Analog optics, analog photonics, Mach–Zehnder modulator, Mach–Zehnder interferometer, microwave filter, instantaneous frequency measurement, binary fiber optic delay lines, phase error, true-time delay, RF photonics.

1. Introduction

Fiber-optic interferometers have proven useful for a wide variety of applications. The Mach–Zehnder interferometer (MZI) is employed for fiber-optic sensors [1], demodulation of digital [2] and analog [3] waveforms imposed on optical carriers, and microwave photonic signal processing [4]–[6]. Recently proposed was an analytical model of filtered microwave photonic links as generalized to both intensity and phase modulation using autocorrelation functions, which was applied to a phase modulated quadrature-biased MZI filter configuration using balanced detection [7]. Here, we present to our best knowledge the most complete analysis of analog electro-optic modulation followed by an asymmetric MZI. Closed-form analytical expressions are derived for the signal response of a link employing a Mach–Zehnder modulator (MZM) and MZI, including the effects of MZM bias, arbitrary coupling ratios in the MZI, and MZI bias. We also review the response of an analog phase modulated link with a MZI [3] for comparison.

The results of the theoretical work are investigated experimentally in the context of three applications. For microwave photonic signal processing techniques, complimentary filter functions result when analog intensity or phase modulation are input to an asymmetric MZI. That is, intensity modulation through a MZI exhibits a positive-tap response whereas phase modulation provides a negative-tap filter. Though both techniques are optically coherent, it is demonstrated that the intensity-modulation response is independent of MZI bias. As first proposed in [8] and demonstrated later in [9], the complementary nature of these responses can be leveraged to increase the

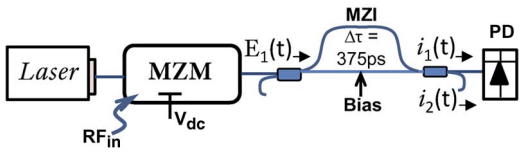

Fig. 1. Architecture for Mach–Zehnder Modulator/Mach–Zehnder Interferometer experiment (Section 2).

unambiguous detection bandwidth of photonic instantaneous frequency measurement (IFM) techniques. Such properties are further investigated here, including important characteristic rejection features. Finally, the theory of a MZM-MZI link is used to analyze the effects of finite optical switch rejection in a binary fiber-optic delay line (BiFODL). The BiFODL architecture is potentially useful in radio-frequency (RF) phased-array applications when implemented with bulk fiber-optic components [10] but especially when using integrated photonic approaches [11].

2. Modulation and Interferometric Detection Theory

2.1. Intensity Modulation

The general setup for this work is a continuous-wave laser coupled to either an electro-optic amplitude [see Fig. 1] or phase modulator, then through a MZI for detection with a photodiode(s). For amplitude modulation using a balanced MZM in the push-pull configuration, the field at its input is $E_{\text{in}}(t) = \kappa\sqrt{2P_{\text{laser}}}e^{i\omega_o t}$, where P_{laser} is the average laser power at angular frequency ω_o and κ is a constant relating field and average power such that $P_{\text{laser}} = E_{\text{in}}^* E_{\text{in}}/(2\kappa^2)$. The input voltage is $v_{\text{in}}(t) = V_{\text{DC}} + V_{\text{rf}}\sin(\Omega t)$, where V_{DC} is the bias voltage and Ω is the angular frequency of the RF signal. In the ideal case of 50/50 optical coupling at the input and output of the MZM, with optical power loss factor of α_{MZM} and net optical gain factor for the link g_o, the field corresponding to a single output can be obtained using the familiar MZM scattering matrices to carry out the transfer, yielding [12]:

$$E_1(t) = \frac{\kappa}{2}\sqrt{2g_o\alpha_{\text{mzm}}P_{\text{laser}}}e^{i\omega_o t}\left[e^{i\phi(t)} - e^{-i\phi(t)}\right] \tag{1}$$

which is also the form representing the field at the input of the MZI, where $\phi(t) = (\phi_{\text{DC}}/2) + (\phi_{\text{rf}}/2)\sin\Omega t$ represents the phase shift produced by the MZM drive voltage in the ideal push-pull configuration. Running the MZM at quadrature bias voltage sets the static shift, $\phi_{\text{DC}} = \pi(V_{\text{DC}}/V_{\pi,\text{DC}}) = \pi/2$, with the analog shift amplitude being $\phi_{\text{rf}} = \pi(V_{\text{rf}}/V_\pi(\Omega))$.

The field from (1) drives the transfer function for the MZI portion of this derivation by setting it as the input to one coupler arm of the MZI, while having the other input coupler arm disconnected nulling its value within the function input. For the purposes of completeness, and serving useful for the BiFODL modeling later, the coupler is not assumed to have a 50% power splitting ratio and thence the 2×2 scattering matrices for the MZI couplers contain a factor η representing the fraction of optical power coupled from input to output. The coupling ratio for the optical field is then $\sqrt{\eta}$ with the corresponding cross coupling ratio equaling $\sqrt{1-\eta}$ (e.g., $\eta = 0.5$ for a coupler with a 50% power splitting ratio, which most MZIs use to achieve the highest extinction ratio) [13]. Then the total associated transfer for the two fields at the MZI output are given by:

$$\begin{bmatrix} E_{o1}(t) \\ E_{o2}(t) \end{bmatrix} = \begin{bmatrix} \sqrt{1-\eta_2} & i\sqrt{\eta_2} \\ i\sqrt{\eta_2} & \sqrt{1-\eta_2} \end{bmatrix} \begin{bmatrix} \Gamma(\tau) & 0 \\ 0 & 1 \end{bmatrix} \begin{bmatrix} \sqrt{1-\eta_1} & i\sqrt{\eta_1} \\ i\sqrt{\eta_1} & \sqrt{1-\eta_1} \end{bmatrix} \begin{bmatrix} E_1(t) \\ 0 \end{bmatrix} \tag{2}$$

where $\Gamma(\tau)$ is a time-delay operator such that $\Gamma(\tau)\cdot E(t) = E(t+\tau)$ with τ being the differential time delay between the two MZI paths. The coupling ratios for the MZI input and output couplers are η_1 and η_2, respectively. Once solving for the fields in (2), the total photocurrent is calculated using the average instantaneous optical power with the formula: $\Re E_o^*(t)E_o(t)/(2\kappa^2)$, with $\Re$ being the

responsivity of the photodiode. Taking the field from one arm of the MZI in (2), $E_{o1}(t)$, inserting it into this formula and using the Jacobi-Anger identities after substitution of $\phi(t)$ as defined above produces the following photocurrent equations:

$$I_{DC} = \frac{1}{4}\Re\zeta^2 \cdot \Bigg\{ \eta_1\eta_2 \cdot (1 - \cos(\phi_{DC})J_0(\phi_{rf})) + (1-\eta_1)(1-\eta_2) \cdot (1 - \cos(\phi_{DC})J_0(\phi_{rf})) - 2[\eta_1\eta_2(1-\eta_1)(1-\eta_2)]^{1/2}\cos(\omega_o\tau) \cdot \left[J_0\left(\phi_{rf}\sin\frac{\Omega\tau}{2}\right) - \cos(\phi_{DC})J_0\left(\phi_{rf}\cos\frac{\Omega\tau}{2}\right)\right]\Bigg\} \tag{3a}$$

$$i(t)_{odd} = \frac{1}{4}\Re\zeta^2 \cdot \Bigg\{ 2\eta_1\eta_2\sin(\phi_{DC}) \cdot \sum_{n=1}^{\infty} J_{2n-1}(\phi_{rf})\sin[(2n-1)\Omega t] + 2(1-\eta_1)(1-\eta_2)\sin(\phi_{DC}) \cdot \sum_{n=1}^{\infty} J_{2n-1}(\phi_{rf})\sin[(2n-1)\Omega(t+\tau)] - 4[\eta_1\eta_2(1-\eta_1)(1-\eta_2)]^{1/2}\cos(\omega_o\tau)\sin(\phi_{DC}) \cdot \sum_{n=1}^{\infty} J_{2n-1}\left(\phi_{rf}\cos\frac{\Omega\tau}{2}\right)\sin\left[(2n-1)\Omega\left(t+\frac{\tau}{2}\right)\right]\Bigg\} \tag{3b}$$

$$i(t)_{even} = -\frac{1}{4}\Re\zeta^2 \cdot \Bigg\{ 2\eta_1\eta_2\cos(\phi_{DC}) \cdot \sum_{n=1}^{\infty} J_{2n}(\phi_{rf})\cos[(2n)\Omega t] + 2(1-\eta_1)(1-\eta_2)\cos(\phi_{DC}) \cdot \sum_{n=1}^{\infty} J_{2n}(\phi_{rf})\cos[(2n)\Omega(t+\tau)] + 4[\eta_1\eta_2(1-\eta_1)(1-\eta_2)]^{1/2}\cos(\omega_o\tau) \cdot \sum_{n=1}^{\infty}\left[(-1)^n J_{2n}\left(\phi_{rf}\sin\frac{\Omega\tau}{2}\right) - \cos(\phi_{DC})J_{2n}\left(\phi_{rf}\cos\frac{\Omega\tau}{2}\right)\right]\cos\left[2n\Omega\left(t+\frac{\tau}{2}\right)\right]\Bigg\} \tag{3c}$$

where J_m are mth-order Bessel functions of the first kind, and $\zeta = [2g_o\alpha_{mzi}\alpha_{mzm}P_{laser}]^{1/2}$ with α_{mzm} being an optical power loss factor for the MZI. Equation (3a) is the DC photocurrent, (3b) is the odd-order RF photocurrent including the output at the fundamental frequencies and (3c) is the even-order RF photocurrent. Applying the small-signal (linear) approximations for Bessel functions which assume that $V_{rf} \ll V_\pi(\Omega)/\pi$, the output photocurrent for the fundamental associated with E_{o1} is:

$$i_1(t)_\Omega = \frac{1}{4}\Re\zeta^2\left(\frac{\phi_{rf}}{2}\right)\sin(\phi_{DC}) \cdot \Bigg\{2\eta_1\eta_2\sin\Omega t + 2(1-\eta_1)(1-\eta_2)\sin[\Omega(t+\tau)] - 4[\eta_1\eta_2(1-\eta_1)(1-\eta_2)]^{1/2}\cos(\omega_o\tau)\cos\frac{\Omega\tau}{2}\sin\left[\Omega\left(t+\frac{\tau}{2}\right)\right]\Bigg\}. \tag{4a}$$

The same procedure is followed for calculating the photocurrent given by field $E_{o2}(t)$; while omitting the total photocurrent for brevity, the isolated fundamental output i_2 is:

$$i_2(t)_\Omega = \frac{1}{4}\Re\zeta^2\left(\frac{\phi_{rf}}{2}\right)\sin(\phi_{DC}) \cdot \Bigg\{2(1-\eta_1)\eta_2\sin\Omega t + 2\eta_1(1-\eta_2)\sin[\Omega(t+\tau)] + 4[\eta_1\eta_2(1-\eta_1)(1-\eta_2)]^{1/2}\cos(\omega_o\tau)\cos\frac{\Omega\tau}{2}\sin\left[\Omega\left(t+\frac{\tau}{2}\right)\right]\Bigg\}. \tag{4b}$$

By using the time-varying current given by (4a) to compute the average RF power, $P_{RF,out} = \langle i(t)_\Omega^2\rangle R_{out}$ delivered to a load with resistance R_{out}, we can determine the gain as

$|S_{21}|^2 = P_{\mathrm{RF,out}}/P_{\mathrm{RF,in}}$ with $P_{\mathrm{RF,in}} = V_{\mathrm{rf}}^2/(2R_{\mathrm{in}})$ and ϕ_{rf} given above, producing:

$$
\begin{aligned}
|S_{21}|^2 = \frac{1}{16}\Re^2\zeta^4\left(\frac{\pi}{V_\pi(\Omega)}\right)^2 \sin^2(\phi_{\mathrm{DC}}) \\
\cdot\Bigg\{(\eta_1\eta_2)^2 + [(1-\eta_1)(1-\eta_2)]^2 + 2\eta_1\eta_2(1-\eta_1)(1-\eta_2)\cos\Omega\tau + 4\cos^2\frac{\Omega\tau}{2} \\
\cdot\Bigg(\eta_1\eta_2(1-\eta_1)(1-\eta_2)\cos^2(\omega_o\tau) - \Big[(\eta_1\eta_2)^3(1-\eta_1)(1-\eta_2)\Big]^{1/2}\cos(\omega_o\tau) \\
- \Big[\eta_1\eta_2[(1-\eta_1)(1-\eta_2)]^3\Big]^{1/2}\cos(\omega_o\tau)\Bigg)\Bigg\} R_{\mathrm{in}}R_{\mathrm{out}}. \qquad (5)
\end{aligned}
$$

where R_{in} is the MZM input resistance that is ideally matched to the driving signal source. In a typical MZI using couplers with 50% power splitting ratios ($\eta_1 = \eta_2 = 0.5$), the maximum S_{21} given by (5) is seen at $\omega_o\tau = (2n+1)\pi$, leaving the minimum at an optical bias of $\omega_o\tau = 2n\pi$.

Furthermore, in a configuration where the fundamental output photocurrents are combined either in summation (Σ) or differential (Δ) detection, the following equations are applicable:

$$
\begin{aligned}
|S_{21}|^2_{\Sigma} = \frac{1}{16}\Re^2\zeta^4\left(\frac{\pi}{V_\pi(\Omega)}\right)^2 \sin^2(\phi_{\mathrm{DC}}) \\
\cdot\Big\{(\eta_1\eta_2)^2 + [(1-\eta_1)(1-\eta_2)]^2 + [\eta_1(1-\eta_2)]^2 + [\eta_2(1-\eta_1)]^2 + 2\eta_1(1-\eta_1)\eta_2^2 \\
+ 2\eta_1(1-\eta_1)(1-\eta_2)^2 + 4\eta_1\eta_2(1-\eta_1)(1-\eta_2)\cos\Omega\tau + 2\eta_2(1-\eta_2)\eta_1^2\cos\Omega\tau \\
+ 2\eta_2(1-\eta_2)(1-\eta_1)^2\cos\Omega\tau\Big\} \cdot R_{\mathrm{in}}R_{\mathrm{out}} \qquad (6a)
\end{aligned}
$$

$$
\begin{aligned}
|S_{21}|^2_{\Delta} = \frac{1}{16}\Re^2\zeta^4\left(\frac{\pi}{V_\pi(\Omega)}\right)^2 \sin^2(\phi_{\mathrm{DC}}) \\
\cdot\Big\{(\eta_1\eta_2)^2 + [(1-\eta_1)(1-\eta_2)]^2 + [\eta_1(1-\eta_2)]^2 + [\eta_2(1-\eta_1)]^2 - 2\eta_1(1-\eta_1)\eta_2^2 \\
- 2\eta_1(1-\eta_1)(1-\eta_2)^2 + 4\eta_1\eta_2(1-\eta_1)(1-\eta_2)\cos\Omega\tau - 2\eta_2(1-\eta_2)\eta_1^2\cos\Omega\tau \\
- 2\eta_2(1-\eta_2)(1-\eta_1)^2\cos\Omega\tau + 8\cos^2\left(\frac{\Omega\tau}{2}\right) \\
\cdot\Big[2\eta_1\eta_2(1-\eta_1)(1-\eta_2)\cdot\cos^2(\omega_o\tau) - \Big[(\eta_1\eta_2)^3(1-\eta_1)(1-\eta_2)\Big]^{1/2}\cos(\omega_o\tau) \\
- \Big[\eta_1\eta_2[(1-\eta_1)(1-\eta_2)]^3\Big]^{1/2}\cos(\omega_o\tau) + \Big[[\eta_2(1-\eta_1)]^3\eta_1(1-\eta_2)\Big]^{1/2}\cos(\omega_o\tau) \\
+ \Big[\eta_2(1-\eta_1)[\eta_1(1-\eta_2)]^3\Big]^{1/2}\cos(\omega_o\tau)\Big]\Big\} \cdot R_{\mathrm{in}}R_{\mathrm{out}}. \qquad (6b)
\end{aligned}
$$

Both (6a) and (6b) become useful later on in Section 4 where we apply the theory.

2.2. Phase Modulation

For application to the photonic filter work later in this paper, we also review the equations for a phase modulated signal through a MZI. With the same $\phi(t)$, $\Gamma(\tau)$, and η as defined in the previous section, the transfer for these two fields is:

$$
\begin{bmatrix} E_{o1}(t) \\ E_{o2}(t) \end{bmatrix} = \frac{\kappa}{2}\sqrt{2g_o\alpha_{\Phi\mathrm{m}}P_{\mathrm{laser}}}\begin{bmatrix} \sqrt{1-\eta_2} & \mathrm{i}\sqrt{\eta_2} \\ \mathrm{i}\sqrt{\eta_2} & \sqrt{1-\eta_2} \end{bmatrix}\begin{bmatrix} \Gamma(\tau) & 0 \\ 0 & 1 \end{bmatrix}\begin{bmatrix} \sqrt{1-\eta_1} & \mathrm{i}\sqrt{\eta_1} \\ \mathrm{i}\sqrt{\eta_1} & \sqrt{1-\eta_1} \end{bmatrix}\begin{bmatrix} \mathrm{e}^{\mathrm{i}(2\phi(t)+\omega_o t)} \\ 0 \end{bmatrix}. \qquad (7)
$$

And once again using the formula $\Re E_o^*(t)E_o(t)/(2\kappa^2)$, the total photocurrent calculation yields:

$$i_{1,2}(t)_\Omega = \frac{1}{4}\Re\zeta'^2 \cdot \Bigg\{(1-\eta_1)(1-\eta_2)+\eta_1\eta_2 \mp 2[\eta_1\eta_2(1-\eta_1)(1-\eta_2)]^{1/2} \cdot \Bigg[\cos(\omega_o\tau)J_0\left(2\phi_{\text{rf}}\sin\frac{\Omega\tau}{2}\right)+2\cos(\omega_o\tau) \cdot \sum_{n=1}^{\infty}(-1)^n J_{2n}\left(2\phi_{\text{rf}}\sin\frac{\Omega\tau}{2}\right)\cos\left[2n\Omega\left(t+\frac{\tau}{2}\right)\right]+2\sin(\omega_o\tau) \cdot \sum_{n=1}^{\infty}(-1)^n J_{2n-1}\left(2\phi_{\text{rf}}\sin\frac{\Omega\tau}{2}\right)\cos\left[(2n-1)\Omega\left(t+\frac{\tau}{2}\right)\right]\Bigg]\Bigg\} \quad (8)$$

where J_m are mth-order Bessel functions of the first kind, and $\zeta' = [2g_o\alpha_{\Phi\text{m}}\alpha_{\text{mzi}}P_{\text{laser}}]^{1/2}$ with $\alpha_{\Phi\text{m}}$ being the optical loss factor of the phase modulator. Moreover, following the same procedure that we exercised for amplitude modulation, the theoretical gain of the phase modulated MZI link is found to be:

$$|S_{21}|^2_{[\Delta]} = [4]\cdot\Re^2\zeta'^4\left(\frac{\pi}{V_\pi(\Omega)}\right)^2\cdot\eta_1\eta_2(1-\eta_1)(1-\eta_2)\cdot\sin^2(\omega_o\tau)\sin^2\left(\frac{\Omega\tau}{2}\right)\cdot R_{\text{in}}R_{\text{out}}. \quad (9)$$

with the coefficient of 4 being a removable factor depending on the measurement of a single MZI output (excludes the coefficient) or the difference of both arms. Summing the fundamental output produces zero photocurrent, and thus $|S_{21}|^2_\Sigma = 0$. Equation (9) will be utilized in Section 4 where we apply the theory.

3. Experimental Validation

Fig. 1 shows the experimental configuration that we used to take network analyzer measurements at a number of different MZI biases from 0 to π, in $\pi/8$ increments, over a broadband frequency spectrum 0–50 GHz, obtaining a data set which validates the theory with confidence. The MZM half-wave voltage V_π was 3.6 V at 1 GHz, and MZI differential delay $\tau = 375$ ps with 50/50 couplers. With the $\omega_o\tau$ set to the appropriate values as specifically measured in (5), and $\Re\zeta^2$ determined experimentally from (3a) at MZM-quadrature, we were able to generate the theoretical curves that correspond to the experimental data over $f = \Omega/2\pi$ as shown in Fig. 2.

From plotting the data [see Fig. 2], we confirm that the theory is well in line with our measurement data. The frequency response of the modulator, $V_\pi(\Omega)$, was determined from a direct-detection link that had a photodiode with known frequency response. Also, note that (5) was multiplied by 1/4 (-6 dB) to account for the loss in the external impedance matching circuit of the photodiode.

4. Applications

4.1. Microwave Photonic Filters

An instance where the derived theory becomes applicable is in link configurations that employ microwave photonic filtering. The tasks of these photonic subsystems are equivalent to those of an ordinary microwave filter within a RF system or link, however with all of the characteristic advantages of photonics such as increased instantaneous bandwidth [14]. Fig. 3 shows a setup that was constructed for taking data from such filters at various MZI biases from 0–20 GHz, with the MZM at quadrature. The optical signal is demodulated with two photodiodes, and a RF hybrid "magic-T" was used to perform the effective waveform math on the exiting RF signal.

For such a link configuration, and with an optimal extinction MZI that has 50/50 optical couplers $(\eta_1 = \eta_2 = 0.5)$, the intensity and phase modulated power expressions from Section 2 reduce to

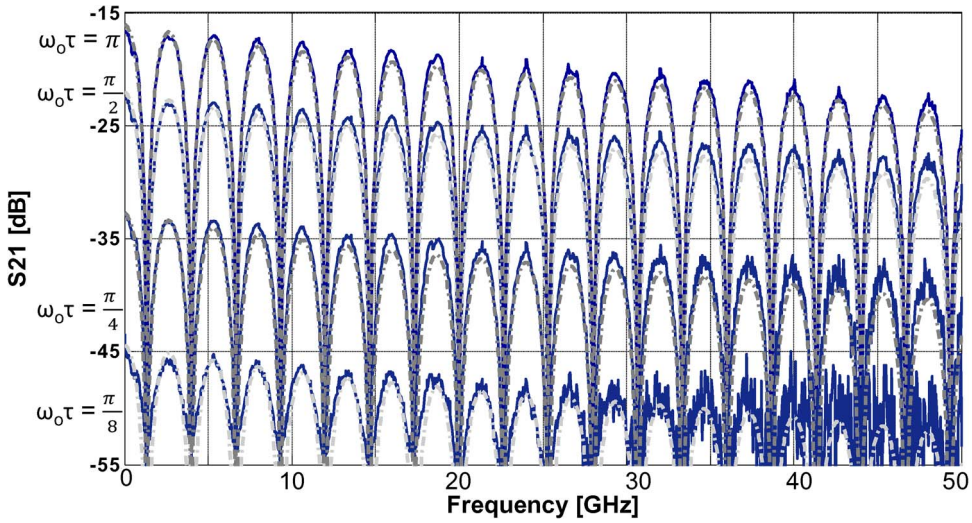

Fig. 2. Theory versus the measurement gain data from our MZM-MZI configuration for several optical biases (labeled to the left of each curve) over a broad frequency spectrum; theoretical curves are the grey dotted lines overlaying the measured data in blue.

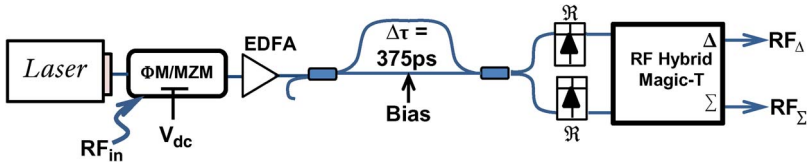

Fig. 3. Experimental setup for phase and intensity modulated photonic filter measurements. Summed and differential data was taken for both the ΦM and MZM schemes.

[(6a), (6b), and (9), respectively]:

$$|S_{21}|^2_{\Sigma mzm} = \frac{1}{16}\Re^2\zeta^4\left(\frac{\pi}{V_\pi(\Omega)}\right)^2 \sin^2(\phi_{DC})\cos^2\left(\frac{\Omega\tau}{2}\right)\cdot R_{in}R_{out}$$

$$|S_{21}|^2_{\Delta mzm} = \frac{1}{16}\Re^2\zeta^4\left(\frac{\pi}{V_\pi(\Omega)}\right)^2 \sin^2(\phi_{DC})\cos^2(\omega_o\tau)\cos^2\left(\frac{\Omega\tau}{2}\right)\cdot R_{in}R_{out}$$

$$|S_{21}|^2_{\Delta\Phi m} = \frac{1}{4}\Re^2\zeta'^4\left(\frac{\pi}{V_\pi(\Omega)}\right)^2 \sin^2(\omega_o\tau)\sin^2\left(\frac{\Omega\tau}{2}\right)\cdot R_{in}R_{out}. \quad (10)$$

Again, $|S_{21}|^2_{\Sigma\Phi m} = 0$ as we noted in Section 2. It becomes apparent from the expressions in (10) that phase and intensity modulation through a MZI exhibit complementary transfer functions, which interleaves their signal responses. This characteristic becomes integral to applications such as IFM as detailed in the next section. Being a function of ϕ_{DC}, these expressions are easily applied to a low or high-bias MZM condition as well as at quadrature, with the emphasis in this experiment on the latter. The theory is validated by these measurements as shown in Figs. 4 and 5. Only one theoretical curve is necessary in the first of these figures for the intensity modulated summation case since we see from both the theory and plot that it provides a positive tap, and while optically coherent, the RF output is evidently independent of the MZI bias. This characteristic of no need for MZI bias control promotes the use of MZM-MZI links in remoted systems. Conversely, phase modulated differential detection is a negative tap that is optically coherent with strong MZI bias dependence because the MZI is required to convert the phase into intensity modulation, which (10) also predicts [see Fig. 5]. V_π was set to 5 V to generate the theoretical data for this experiment.

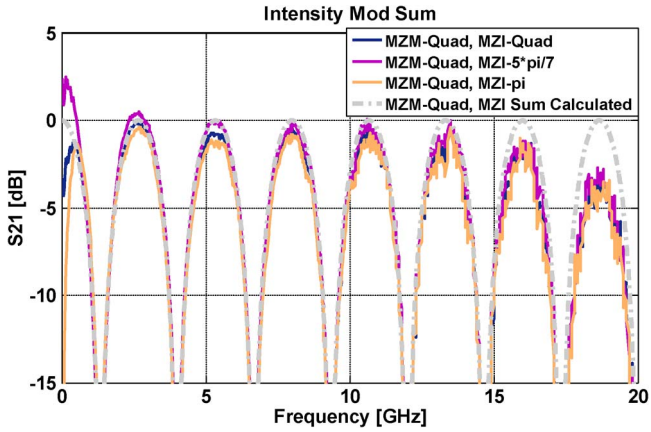

Fig. 4. Intensity modulated photonic filter measurements using RF hybrid Magic-T versus Theoretical Data, theory and measurements all normalized to zero.

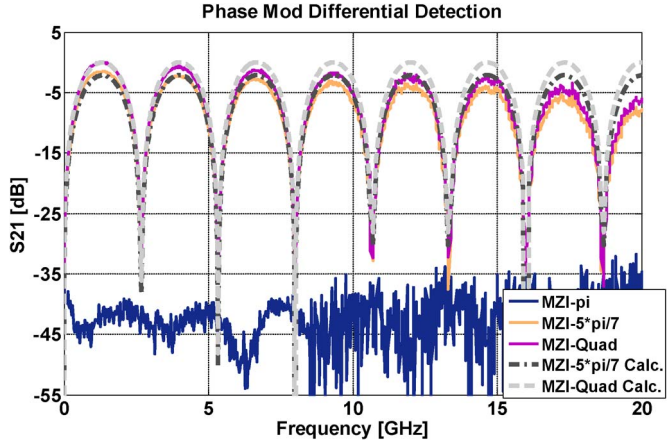

Fig. 5. Phase modulated photonic filter differential detection measurements using RF hybrid Magic-T versus Theoretical Data, both normalized to zero.

$V_\pi(\Omega)$ was not explicitly determined which is indicated by less agreement with the measurements as they roll-off due to this frequency dependence.

4.2. Instantaneous Frequency Measurement

The capability to identify the dominant frequency of an unknown microwave signal in near-real time, over a wide bandwidth (near DC to $>$ 100 GHz) and with high resolution ($<$ 500 MHz) is of particular interest to electronic warfare applications. Recent photonics-based IFM solutions are promising over conventional techniques that suffer from stringent bandwidth size tradeoffs. Post-filter processing allows for frequency resolution well below the filter narrow 3-dB bandwidth $(\mathrm{BW}_{3\,\mathrm{dB}})$. This approach also circumvents the unresolved issues in realizing these narrow pass bands over large processing bandwidths (large free-spectral range, FSR), and with high-sensitivity, of the more straightforward photonic approach that uses optical or microwave-photonic filters to conduct wideband down conversion and/or channelization of a RF-modulated optical signal [8], [15]–[17].

Through this work, we now have the closed-form expressions for the complementary power responses seen within the IFM technique suggested by [8] that employs two optically coherent microwave photonic filters, a simultaneous phase and intensity modulation format where an amplitude comparison function (ACF) is ultimately constructed yielding an unambiguous detection

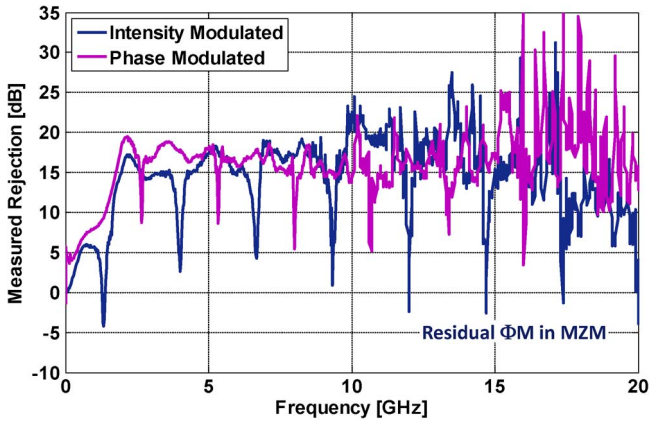

Fig. 6. Measured link rejection.

bandwidth of $1/(2\tau)$. These two filters consist separately of a phase modulator and a quadrature-biased MZM, both followed by a single asymmetric MZI with 50/50 optical couplers having a differential time delay τ and four photodiodes at its output (one balanced pair and one additive pair). With the MZI specifically quadrature-biased, the expressions in (10) reduce to:

$$
\begin{aligned}
|S_{21}|^2_{\Sigma mzm} &= \frac{1}{16}\Re^2\zeta^4\left(\frac{\pi}{V_\pi(\Omega)}\right)^2\cos^2\left(\frac{\Omega\tau}{2}\right)\cdot R_{in}R_{out}\\
|S_{21}|^2_{\Delta mzm} &= 0\\
|S_{21}|^2_{\Sigma\Phi m} &= 0\\
|S_{21}|^2_{\Delta\Phi m} &= \frac{1}{4}\Re^2\zeta'^4\left(\frac{\pi}{V_\pi(\Omega)}\right)^2\sin^2\left(\frac{\Omega\tau}{2}\right)\cdot R_{in}R_{out}.
\end{aligned}
\tag{11}
$$

The theory specified in (11) predicts that a MZI employing balanced detection demodulates phase modulation and rejects optical intensity modulation at its input; while a MZI utilizing additive photodetection of its outputs demodulates intensity modulation and rejects phase modulation. This characteristic is critical to the simultaneous intensity and phase modulation IFM technique mentioned here. A measurement of this rejection is plotted in Fig. 6, which was determined by taking the difference at MZI quadrature bias of the minimum from the maximum response for both phase and intensity modulation. While showing decent rejection, the intensity modulation response exhibits some residual phase modulation, or chirp. Non-ideal rejection can also be caused by amplitude and/or phase mismatch of the two outputs. Phase mismatch caused by a true time delay error can be ruled out in this case because the rejection would get worse with frequency.

However, despite what the theory predicts, when we took phase modulation photocurrent summation measurements there was some residual gain seen in the filter. Phase modulators have been shown to exhibit parasitic intensity modulation (PIM) as a result of fabrication imperfections, with two fundamental sources being induced by mode-mismatch loss variation, and propagation loss variation; additionally, residual optical reflections can create an interferometric-effect amplitude modulation within the modulator when using a laser source with a long coherence length [18].

4.3. Binary Fiber-Optic Delay Line

Another important application of microwave photonics is for true time delay beamsteering of antenna arrays. A photonic true time delay system for feeding an array of antennas is based on the use of broadband photonic delay lines [10], [14]. A BiFODL can be implemented in such a system using switches where minimal crosstalk is desired. The setup shown in Fig. 7 was assembled to measure levels of crosstalk in the form of phase error (PE), where one arm of the MZI was heavily

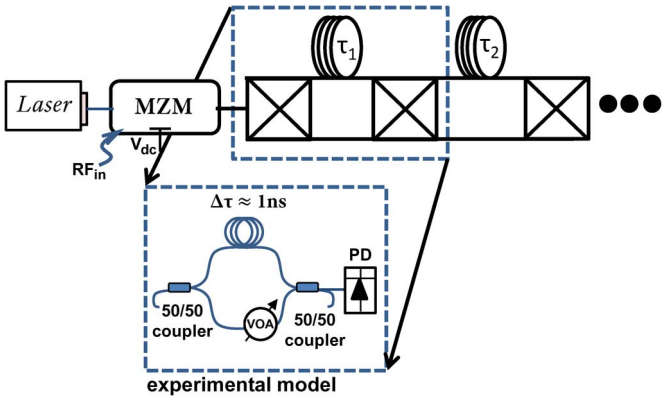

Fig. 7. BiFODL configuration and experimental setup. The crosstalk represented as phase error was measured at several relative attenuations of 20, 30, 40, and 50 dB.

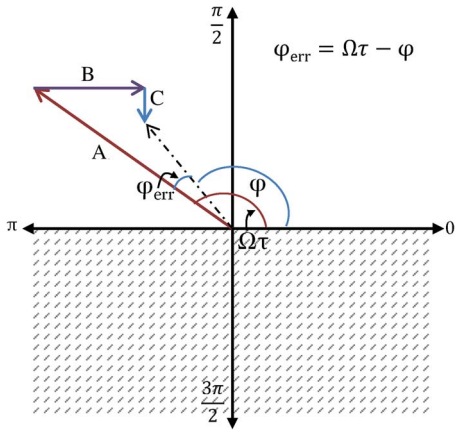

Fig. 8. Schematic MZI phase error representation. Vectors A, B, and C are the amplitudes of the corresponding signal component and φ_{err} is phase error. To keep the translation simple, the phase of A was restricted to Quadrants I & II, rotating A back by π when necessary.

attenuated mimicking a 2 $\times$ 2 switch. To model 10 dB switch extinction, a relative attenuation of 20 dB was applied to the straight arm of the MZI; and then similarly for 15, 20, and 25 dB extinction. The MZM was run at quadrature within this experiment.

The BiFODL experimental setup was calibrated to the delay arm of the MZI where the straight arm was disconnected for calibration and reconnected to make the PE measurements. Fig. 8 is a schematic representation of PE where the magnitudes of vectors A, B, and C are defined by the photocurrent amplitudes of the desired and interference signal components. The magnitude of vector A, representing the delay component of the system, is found by setting the 1 to a 0 in the time-delay operator matrix of (2) as if there were no signal from the straight arm of the MZI. This becomes the desired signal with amplitude A, and the resulting photocurrent expression is:

$$i(t)_{\Omega\tau} = A\sin[\Omega(t+\tau)]$$

where

$$A = \frac{1}{4}\Re\zeta^2\left(\frac{\phi_{rf}}{2}\right)\cdot 2(1-\eta_1)(1-\eta_2). \tag{12}$$

We find this desired signal as a component of the total output photocurrent for this configuration where it is precisely the second term in (4a). The remaining terms then comprise the interference

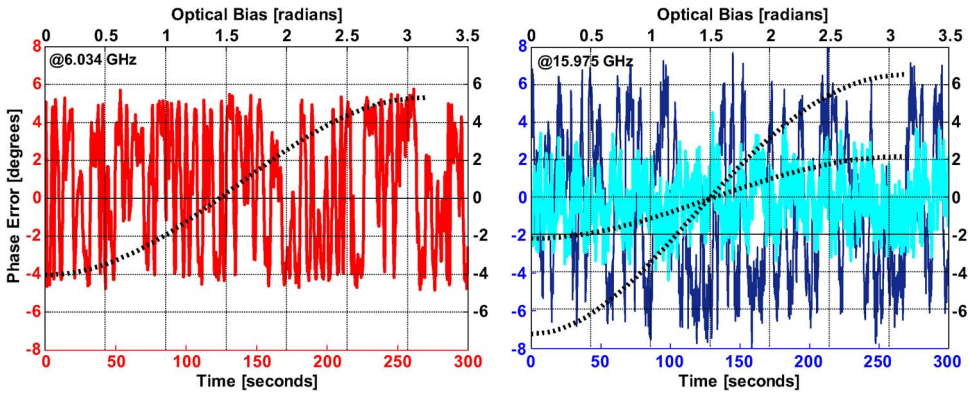

Fig. 9. (Left) Phase error at 6.034 GHz, 20 dB relative attenuation. (Right) Phase error at 15.975 GHz, 20 dB (dark blue) and 30 dB (cyan) relative attenuations. The black curves overlaid represent the theoretical phase error swing.

signal and after separating (12), (4a) is rearranged to be in a form more conducive to this vector analysis, where this interference signal that arises from the finite extinction of the switch can be written as having both an in-phase and quadrature component:

$$i(t)_{\Omega t} = B\sin\Omega t - C\cos\Omega t$$

where

$$B = \frac{1}{2}\Re\zeta^2\left(\frac{\phi_{\text{rf}}}{2}\right)\cdot\left[\eta_1\eta_2 - 2[(\eta_1\eta_2(1-\eta_1)(1-\eta_2)]^{1/2}\cos(\omega_o\tau)\cos^2\left(\frac{\Omega\tau}{2}\right)\right]$$
$$C = \Re\zeta^2\left(\frac{\phi_{\text{rf}}}{2}\right)\cdot[(\eta_1\eta_2(1-\eta_1)(1-\eta_2)]^{1/2}\cos(\omega_o\tau)\cos\left(\frac{\Omega\tau}{2}\right)\sin\left(\frac{\Omega\tau}{2}\right). \quad (13)$$

From here, basic vector trigonometry as depicted in Fig. 8 using the magnitudes of A, B, and C, and where the initial phase of the desired signal is $\Omega\tau$, produces the resulting theoretical PE.

As was mentioned in Section 2, the coupling ratio for the theory was not assumed to be 50% which becomes important here in modeling the BiFODL. While the value of η_1 remains 0.5, η_2 varies with the level of attenuation applied to the straight arm. So for a 20 dB relative attenuation, the delay arm has effectively 100$\times$ the power and as such the following equation is used to define and calculate η_2:

$$\eta_2 = \frac{P_{o2}}{P_{o1}+P_{o2}} = \frac{P_{o2}}{\frac{1}{10^{\left(\frac{P_{\text{att}}}{10}\right)}}\cdot P_{o2}+P_{o2}} = \frac{10^{\left(\frac{P_{\text{att}}}{10}\right)}}{1+10^{\left(\frac{P_{\text{att}}}{10}\right)}} \quad (14)$$

where P_{o1} and P_{o2} represent the output power of each arm of the coupler, and P_{att} is the attenuation in dB. Substituting $P_{\text{att}} = -20$ dB into (14), we return an $\eta_2 = .0099$; similarly -30 dB results in $\eta_2 = .00099$. Because the MZI optical bias could not be fixed, the PE was fluctuating over a range of frequencies. So rather than look at the PE over a spectrum, the sampling was instead centered at one frequency over a period of five minutes to gather enough data for a comprehensive picture of the PE at that frequency. Using the vector math described above, the PE was calculated as a function of optical bias to obtain the range of PE at a certain frequency and attenuation [see Fig. 9].

The plots of Fig. 9 are at two frequencies both containing data for 10 dB switch extinction, while the chart on the right also shows comparison data at 15 dB extinction. As expected the PE decreases with more attenuation, and increases with frequency. It is evident that the theory is again in good agreement with the sampling data. Accordingly, this methodology provides a sound model for estimating PE in a BiFODL where, in regard to beamforming applications, phase error is to be optimally minimized.

5. Conclusion

Presented is a thorough analysis of tandem analog electro-optic modulation and interferometric detection. Closed-form analytical expressions for the signal response of links that employ either phase or intensity modulation and an asymmetric MZI have been provided, as well as a study of the effects of MZM/MZI bias and arbitrary coupling ratios as they pertain to several applications. The MZI is a vital component for the demodulation of digital and analog waveforms imposed on optical carriers, and is incorporated in fiber-optic sensors as well as microwave signal processing such as the IFM technique described. The analysis here focuses on the signal transfer of the single-tone fundamental response, to include the closed-form expressions for even and odd-order harmonic distortions representing the nonlinearity that evolves in these links. Similar expressions can be derived for multiple tones which would produce intermodulation distortion terms, and further the conventional intercept points. Noise considerations such as thermal and shot noise of such links are straightforward. System metrics such as noise figure, spurious free dynamic range (SFDR) and compression dynamic range require further noise measurement and analysis not presented here, such as the calculation of the third-order output intercept point (OIP3). It is also important to consider the coherence length of the noise source through the MZI that originates from signal amplification and optical lasers. The theory introduced here is validated in both the frequency and time domain, where various measurements show good agreement with the calculations, proving to be a solid model for predicting the behavior of similar analog optical systems.

References

[1] A. Dandridge, "Fiber optic sensors based on the Mach–Zehnder and Michelson interferometers," in *Fiber Optic Sensors: An Introduction for Engineers and Scientists*, E. Udd and W. B. Spillman, Eds. 2nd ed. Hoboken, NJ, USA: Wiley, 2011.

[2] A. H. Gnauck and P. J. Winzer, "Optical phase-shift-keyed transmission," *J. Lightw. Technol.*, vol. 23, no. 1, pp. 115–130, Jan. 2005.

[3] V. J. Urick, J. D. McKinney, J. F. Diehl, and K. J. Williams, "Equations for two-tone analog optical phase modulation with an asymmetric interferometer," *IEEE Photon. Technol. Lett.*, to be published.

[4] R. A. Minasian, "Photonic signal processing of microwave signals," *J. Lightw. Technol.*, vol. 54, no. 2, pp. 832–846, Feb. 2006.

[5] J. Yao, "Microwave photonics," *J. Lightw. Technol.*, vol. 27, no. 3, pp. 314–335, Feb. 2009.

[6] J. Capmany, J. Mora, I. Gasulla, J. Sancho, J. Lloret, and S. Sales, "Microwave photonic signal processing," *J. Lightw. Technol.*, vol. 31, no. 4, pp. 571–586, Feb. 2013.

[7] I. Gasulla and J. Capmany, "Analytical model and figures of merit for filtered microwave photonic links," *Opt. Exp.*, vol. 19, no. 20, pp. 19 758–19 774, Sep. 2011.

[8] V. J. Urick, J. D. McKinney, J. F. Diehl, and J. M. Singley, "Simultaneous optical phase and intensity modulation for analog signal processing," presented at the IEEE AVFOP Conf. Dig., Piscataway, NJ, USA, Oct. 2011, Paper TuD4.

[9] D. Wang, K. Xu, J. Dai, Z. Wu, L. Gui, Y. Li, and J. Lin, "A photonic approach for instantaneous microwave frequency measurement based on simultaneous phase modulation and intensity modulation using Mach–Zehnder interferometers," in *Proc. Int. High Speed Intell. Commun. Forum*, May 2012, pp. 1–3.

[10] A. P. Goutzoulis, D. K. Davis, and J. M. Zomp, "Prototype binary fiber optic delay line," *Opt. Eng.*, vol. 28, no. 11, pp. 1193–1202, Nov. 1989.

[11] S. Fathpour and N. A. Riza, "Silicon-photonics-based wideband radar beamforming: Basic design," *Opt. Eng.*, vol. 49, no. 1, pp. 018201-1–018201-7, Jan. 2010.

[12] V. J. Urick, F. Bucholtz, J. D. McKinney, P. S. Devgan, A. L. Campillo, J. L. Dexter, and K. J. Williams, "Long-haul analog photonics," *J. Lightw. Technol.*, vol. 29, no. 8, pp. 1182–1205, Apr. 2011.

[13] R. Hui and M. O'Sullivan, *Fiber Optic Measurement Techniques*. Burlington, MA, USA: Elsevier, 2009.

[14] J. Capmany, B. Ortega, and D. Pastor, "A tutorial on microwave photonic filters," *J. Lightw. Technol.*, vol. 24, no. 1, pp. 201–229, Jan. 2006.

[15] X. Zhang, H. Chi, X. Zhang, S. Zheng, X. Jin, and J. Yao, "Instantaneous microwave frequency measurement using an optical phase modulator," *IEEE Microw. Wireless Compon. Lett.*, vol. 19, no. 6, pp. 422–424, Jun. 2009.

[16] N. Sarkhosh, H. Emami, L. Bui, and A. Mitchell, "Reduced cost photonic instantaneous frequency measurement system," *IEEE Photon. Technol. Lett.*, vol. 20, no. 18, pp. 1521–1523, Sep. 2008.

[17] J. Niu, S. Fu, K. Xu, J. Zhou, S. Aditya, J. Wu, and P. P. Shum, "Instantaneous microwave frequency measurement based on amplified fiber-optic recirculating delay loop and broadband incoherent light source," *J. Lightw. Technol.*, vol. 29, no. 1, pp. 78–84, Jan. 2011.

[18] R. Tavlykaev, A. O. J. Wiberg, G. K. Gopalakrishnan, and S. Radic, "Nonlinear distortions in EO phase modulators," *IEEE Photon. Technol. Lett.*, vol. 24, no. 19, pp. 1778–1780, Oct. 2012.